Supporting Information

A copper coordination polymer precatalyst with asymmetric building units for selective CO_2-to-C_2H_4 electrolysis

Chun Fang Wen,[a] Min Zhou,[b] Xuefeng Wu,[a] Yuanwei Liu,[a] Fangxin Mao,[a] Huai Qin Fu,[c] Yingli Shi,[a] Sheng Dai,[d] Minghui Zhu,[e] Shuang Yang,[a] Hai Feng Wang,[b] Peng Fei Liu*[a] and Hua Gui Yang*[a]

[a] Key Laboratory for Ultrafine Materials of Ministry of Education, Shanghai Engineering Research Center of Hierarchical Nanomaterials, School of Materials Science and Engineering, East China University of Science and Technology, 130 Meilong Road, Shanghai 200237, China.

[b] Key Laboratory for Advanced Materials, School of Chemistry and Molecular Engineering, East China University of Science and Technology, 130 Meilong Road, Shanghai 200237, China.

[c] Centre for Catalysis and Clean Energy, Gold Coast Campus, Griffith University, Gold Coast, QLD 4222, Australia.

[d] Key Laboratory for Advanced Materials and Feringa Nobel Prize Scientist Joint Research Center, Institute of Fine Chemicals, School of Chemistry and Molecular Engineering, East China University of Science and Technology, 130 Meilong Road, Shanghai 200237, China.

[e] State Key Laboratory of Chemical Engineering, School of Chemical Engineering, East China University of Science and Technology, 130 Meilong Road, Shanghai 200237, China.

*E-mail address: hgyang@ecust.edu.cn (H. G. Yang); pfliu@ecust.edu.cn (P. F. Liu)

Methods

Materials. All chemicals and solvents were used without any purification. Copper nitrate trihydrate ($Cu(NO_3)_2 \cdot 3H_2O$) was bought from Aladdin, isopropyl alcohol (AR, ≥99.0%), potassium hydroxide (KOH) and potassium bicarbonate ($KHCO_3$) were purchased from Shanghai Lingfeng Chemical Reagent. Benzene-1,3,5-tricarboxylate (H_3BTC) was obtained from Shanghai Macklin Biochemical Co., Ltd. Ethanol was bought from Shanghai Titan Scientific Co., Ltd. Dimethyl sulphoxide and Nafion solution (5 wt%) were purchased from Sigma-Aldrich. Deuterium water (D_2O) was bought from J&K. Carbon dioxide (CO_2, 99.9999%) and High purity argon (Ar, 99.9%) gases were provided by the Shanghai Jiajie Special Gas Co., Ltd. Carbon papers (Sigracet 28BC) was obtained from the fuel cell store. FAB-PK-130 was obtained from Fuel Cell Store. The deionized water (>18.25 MΩ cm) used in our experiments was provided by Millipore System (Millipore, Billerica, MA).

Synthesis of HKUST-1. $Cu(NO_3)_2 \cdot 3H_2O$ (5.50 g) and H_3BTC (2.45 g) were dissolved in the mixed solution of 40 mL deionized water and 40 mL ethanol, respectively. Then, the above two solutions were mixed and stirred for 1 hour at room temperature. Afterward, the blue suspension solution was transferred into a Teflon-lined autoclave, sealed and kept at 100 °C for 24 hours. As-synthesized HKUST-1 was collected by centrifugation and washed several times with ethanol, and dried overnight in a vacuum oven at 60 °C.

Synthesis of Cu-BTC-CP. 500 mg as-synthesized HKUST-1 was added to 35 mL deionized water with continuous stirring for 3 min at room temperature. Afterward, the

above solution was transferred into a Teflon-lined autoclave, sealed and kept at 180 °C for 4 hours. The sample in the reactor was collected by centrifugation and washed several times with deionized water, and dried overnight in a vacuum oven at 60 °C. Samples of Cu-BTC-CP (2h) and Cu-BTC-CP (12h) were synthesized using the same method, whereby the reaction time of 4 hours was replaced by 2 and 12 hours.

Characterization.

The morphology of the catalyst was collected using scanning electron microscopy (SEM) on a Hitachi S4800, transmission electron microscopy (TEM) on JEOL JEM 2010 with an acceleration voltage of 200 kV and scanning transmission electron microscopy (STEM) on Thermo Fisher Talos F200X. High angle annular dark field (HAADF)-STEM images were recorded using a convergence semi-angle of 11 mrad, and inner- and outer collection angles of 59 and 200 mrad, respectively. Energy dispersive X-ray spectroscopy (EDS) was carried out using 4 in-column Super-X detectors. The X-ray diffraction (XRD, D/max2550V) patterns were recorded using Cu Kα radiation (λ = 1.5406 Å, scan rate = 5° min^{-1}). The chemical composition was analyzed on X-ray photoelectron spectroscopy (XPS, Thermo Escalab 250) with Al Kα X-ray beam (1,486.6 eV), and XPS spectra was calibrated with C 1s peak at 284.8 eV as the reference. Fourier transform infrared (FTIR) spectra was carried out on a Nicolet 6700 spectrometer with a spectral range of 400-4000 cm^{-1}. Brunauer-Emmett-Teller (BET) surface area was calculated from N_2-physisorption measurements on a Micromeritics ASAP 2460. TG profiles were obtained from a TG209F1 thermogravimetric analyzer from 28 to 800 °C with a heating rate of 10 °C min^{-1} in air

flow. The XAFS spectra were collected at the beamline of 1W1B station in Beijing Synchrotron Radiation Facility (BSRF), China. XAFS measurements at the Cu K-edge were recorded in a fluorescence mode using a Lytle detector. Cu foil, Cu_2O and CuO were used as references. The sample was collected several times to obtain high-quality data. The acquired EXAFS data were processed according to the standard procedures using the ATHENA module implemented in the IFEFFIT software packages.

In situ Raman was collected in the homemade flow cell using a Leica DMLM microscope (Renishaw) with a 633 nm laser. The electrochemical CO_2 reduction was performed at different potentials from –0.8 to –1.8 V vs. RHE in CO_2-saturated 0.1 M $KHCO_3$ on samples. The high-purity CO_2 (99.9999%) gas continuously flowed at an average rate of 20 mL min^{-1} into the configuration during electrochemical measurement. A 633 nm laser was taken as the light source to shine directly on the catalyst surface, and a computer synchronously collected the Raman signals.

Electrochemical measurements.

All electrochemical measurements were carried out a CHI760E electrochemical station. An Ag/AgCl (saturated KCl) was used as reference electrode. A mass flow controller was used to control the flow rate of CO_2 to 20 mL min^{-1}. All the potentials in this work were converted to the reversible hydrogen electrode (RHE) based on the following equation, E (vs. RHE) = E (vs. Ag/AgCl) + 0.205 V + 0.059 × pH (all potentials were not *iR*-corrected if not mentioned).

Electrolysis in H cell. The H cell consists of two compartments separated by a Nafion-

117 proton exchange membrane, and each compartment contained 30 mL of 0.1 M $KHCO_3$ electrolyte. Before electrochemical test, 0.1 M $KHCO_3$ catholyte was saturated with CO_2 by bubbling CO_2 gas for at least 0.5 h. The pH value of CO_2 saturated 0.1 M $KHCO_3$ catholyte is around 6.80. The glassy carbon electrode loaded with the catalysts served as working electrode. A platinum mesh was used as counter electrode.

Preparation of working electrode. For the H cell, the sample ink was prepared by ultrasonically dispersing 10 mg catalyst (Cu-BTC-CP or HKUST-1) and 80 μL Nafion solution (5 %) into 1 mL iso-propanol for 0.5 h. Then, 5 μL ink was drop-coated on the glassy carbon electrode with a diameter of 3 mm and a surface area of 0.07 cm^2. The electrode was then dried slowly at room temperature for subsequent testing.

Electrolysis in flow cell. A catalyst-decorated gas-diffusion electrode served as working electrode. A nickel foam was used as counter electrode. 1.0 M KOH aqueous solution was used as electrolyte, which was circulated through the cathode and anode chambers at a rate of 10 ml min^{-1} by a two-channel peristaltic pump. The linear sweep voltammetry (LSV) with a scan rate of 10 mV s^{-1} was obtained in 1.0 M KOH electrolyte. Electrochemical impedance spectroscopy (EIS) measurement was conducted by applying at –0.40 V (vs. RHE) with frequency ranges from 10^5 Hz to 0.001 Hz and 5 mV amplitude.

Preparation of working electrode. For flow cell, the sample ink was prepared by ultrasonically dispersing of 20 mg catalyst (Cu-BTC-CP or HKUST-1) and 80 μL Nafion solution (5 %) into 2 mL iso-propanol for 0.5 h. Then, 2 mL ink was sprayed onto the gas diffusion layers (Sigracet 28BC) with the size of 2×5 cm^2. The electrode

was then dried at 60°C for 1 h before operation.

Pretreatment of nickel foam. The commercially available nickel foam was sonicated with acetone, and ethanol for 15 min, respectively. Then, the nickel foam was immersed in 3.0 M hydrochloric acid solution for 15 min. Finally, the nickel foam was washed by deionized water and ethanol for several times. The obtained nickel foam was dried at 60 °C in a vacuum oven for the subsequent testing.

Products analysis.

The gaseous products were quantitatively analyzed using gas chromatography (GC, RAMIN, GC2060), equipped with a thermal conductivity detector (TCD for H_2) and a flame ionization detector (FID for CO, CH_4 and C_2H_4). Argon was used as the carrier gas. The CO_2 gas was continuously purged at a flow rate of 20 mL min^{-1} into the cathodic compartment and was routed into the GC. The liquid products (like HCOOH, CH_3OH, C_2H_5OH, CH_3COOH etc.) were quantified by using ^1H nuclear magnetic resonance (NMR) (Varian 700MHz spectrometer, 16.4 T) with H_2O suppression. In a typical analysis, 100 μL of the electrolyte was mixed with 500 μL of D_2O solution, and dimethylsulfoxide was used as an internal standard. The data processing of the NMR spectra was performed using the Bruker software TopSpin.

For gas products, the Faradaic efficiency was calculated as follows.

$$FE_{gas} = \frac{nFvGP_0}{i_{total}RT} \times 100\%$$

Where v = volume concentration of species gas measured by GC data. T (K) is the ambient temperature of the test, G is the CO_2 flow rate at room temperature and ambient

pressure. i_{total} (mA) is the steady-state total current, P_0 = 1.013 Pa, F = 96485 C mol^{-1}, R = 8.314 J mol^{-1} K^{-1}. n = the number of electrons transferred for reduction products.

For liquid products, the following method was used for the calculation of Faradaic efficiency. The area ratio of the liquid products peak to the DMSO peak was compared to the standard curve to quantify the concentration of liquid products. The molar quantity of liquid products (X_{liquid}) was calculated via multiplying the concentration of liquid products with the volume of the catholyte.

$$FE_{liquid} = \frac{nFX_{liquid}}{i_{total}\,t} \times 100\%$$

Where i_{total} (mA) is the steady-state total current, n = the number of electrons transferred for reduction products, F = 96485 C mol^{-1}, t is the CO_2 electrolysis time.

DFT calculations details.

All the spin-polarized calculations were performed with the Vienna Ab-initio Simulation Package (VASP)[1, 2] package, using the Perdew-Burke-Ernzerhof (PBE) functional[3] within the generalized gradient approximation (GGA).[4] The project-augmented wave (PAW) method[5] was used to represent the core-valence electron interaction. The valence electronic states were expanded in plane wave basis sets with a cutoff energy of 450 eV. The van der Waals interaction was considered using the DFT-D3 method.[6]

The Cu(111) surface charactering with a coordination number (CN) of 9 were constructed using a p(4 × 4) unit cells with four layers. To ascertain the model in the Cu matrix with a CN of 8, the Cu(111) surface with one Cu vacancy was constructed.

For comparison, we also model the Cu(111) surface with a linear defect, which contains Cu site with a CN of 7. A vacuum layer of 13 Å was applied to separate each periodic unit cell. The bottom two layers of all models were fixed, and a corresponding (2×2×1) mesh was utilized for all structure optimizations. The transition states (TSs) were searched by a constrained optimization scheme[7, 8] and the convergence of forces was set to 0.05 eV/Å.

When involving $H^+ + e^-$ in the elementary step of the CO_2 electrocatalytic reaction, we consider the reference potential to be that of the standard hydrogen electrode (SHE). Then, one can relate the chemical potential for $H^+ + e^-$ to that of 1/2 H_2 in the gas phase at the condition (pH = 0, p_{H2} = 1, T = 298 K and U = 0 V).[9] The adsorption energies of pertinent adsorbates are defined as follows: $E_{ads} = E_{(adsorbate+surface)} - E_{(adsorbate)} - E_{(surface)}$, where $E_{(adsorbate)}$, $E_{(adsorbate\ +\ surface)}$, and $E_{(surface)}$ are the chemical potential of free adsorbate in gas/liquid phase, the total energies of the adsorbates binding to surface, and clean surface, respectively. The more negative the E_{ads} value is, the more strongly the adsorbate binds on the surface. For the adsorption/desorption processes, the large entropy contributions of gaseous molecules (TΔS), including the vibrational, rotational, and translational entropies, have to be considered to estimate the free energy change of the elementary step ΔG at a temperature of 298 K. The Gibbs free energy change (ΔG) of adsorption/desorption processes is estimated according to ΔG = ΔH – TΔS. The reaction enthalpy ΔH is approximated with the total energy difference (ΔE) neglecting the small zero-point energy correction (ΔZPE), heat capacity correction and Δ(pV) term.

Noticeably, to consider the solvent effect, the molecular dynamics (MD) calculations were performed using the model with the perfect Cu(111) and the Cu(111) surfaces with defect (point or line defect), in which lattice-matching pure bulk ice (containing 12 H_2O and 22 H_2O molecules, respectively) was applied above the surface as an initial aqueous network at the liquid/solid interface. Only the Γ point was used to sample the Brillouin zone. The simulation temperature was set to 300 K (experimental temperature) with a 1 fs movement for each step in the canonical (NVT) ensemble employing Nosé-Hoover thermostats. Nearly 8 ps MD simulations were performed, and all the simulations reach the equilibrium plateau after ~ 4 ps.

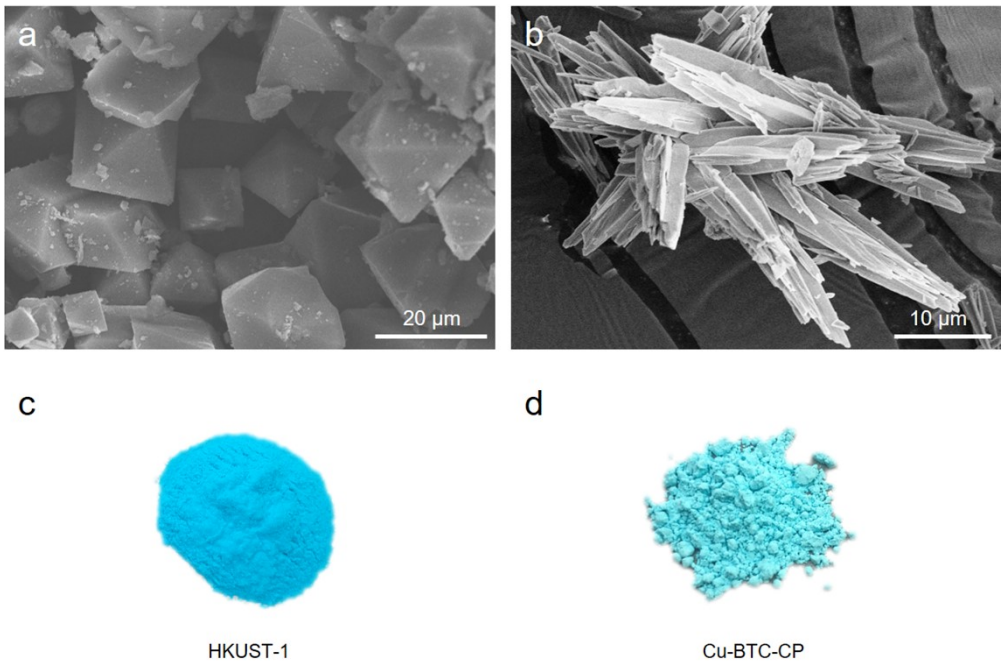

Fig. S1. SEM images of (a) HKUST-1 and (b) Cu-BTC-CP, respectively. HKUST-1 exhibits an octahedral morphology, while Cu-BTC-CP has an irregular rod-like shape. The digital photos of (c) HKUST-1 and (d) Cu-BTC-CP.

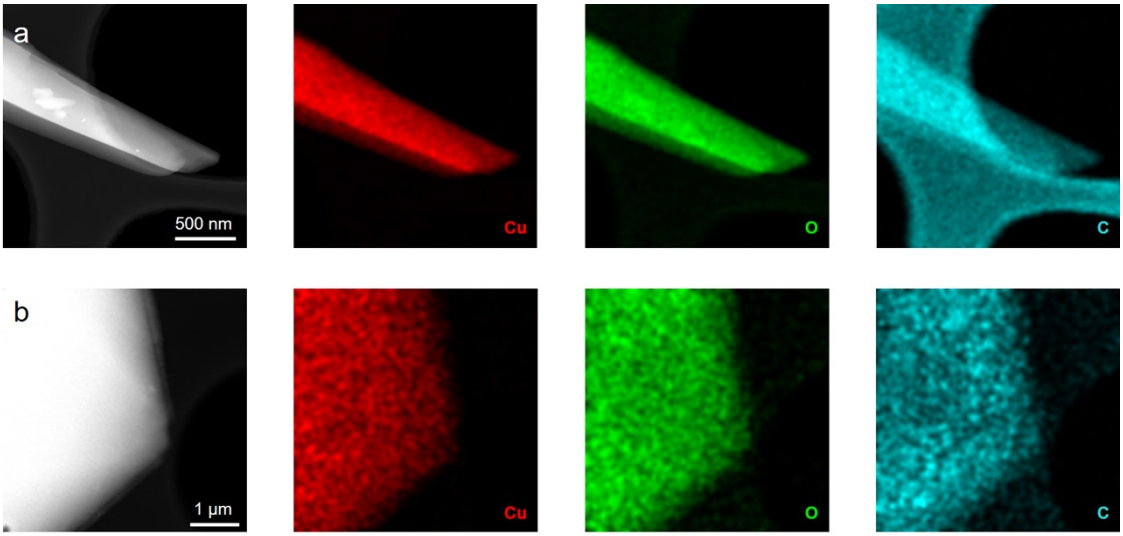

Fig. S2. HAADF-STEM images for (a) Cu-BTC-CP and (b) HKUST-1 and corresponding EDS elemental maps of Cu, O and C.

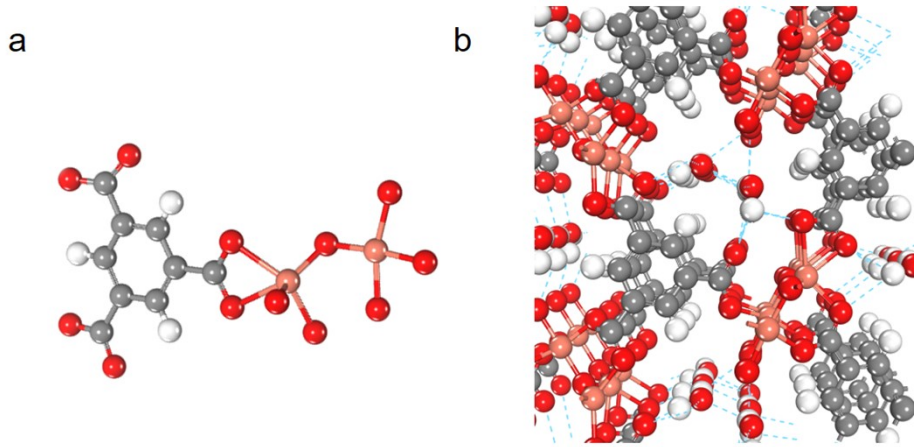

Fig. S3. (a, b) Schematic model of the coordination structure for Cu atoms and tricarboxylic ligand in Cu-BTC-CP. The color scheme for chemical representation: orange, red, gray, and white balls refer to Cu, O, C, H.

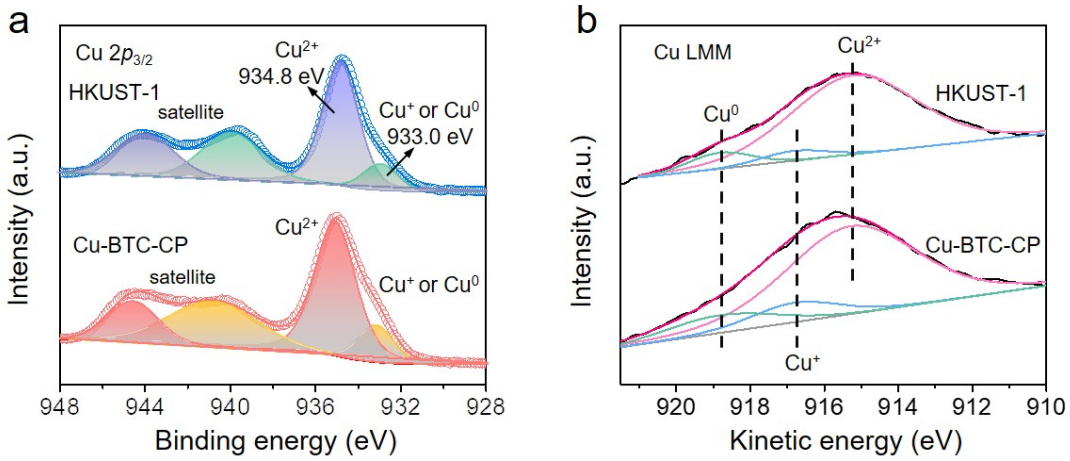

Fig. S4. (a) Cu 2*p* high-resolution XPS spectra and (b) Cu LMM Auger spectra of HKUST-1 and Cu-BTC-CP samples. It is noted that the conversion of Cu^{2+} to low-valent Cu in MOF is induced by the exposure of MOF to an X-ray source and charge neutralizer during data collection.[10]

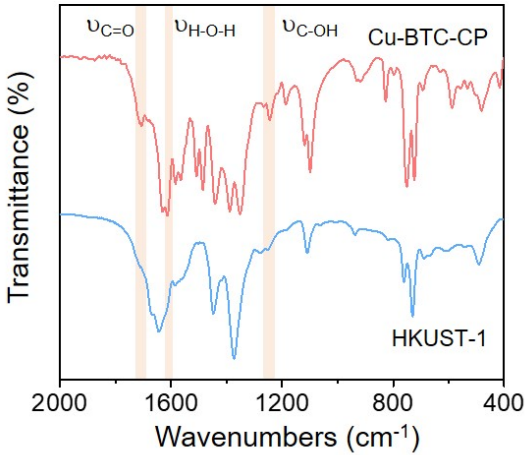

Fig. S5. FTIR spectra of Cu-BTC-CP and HKUST-1 in a spectral range of 600 cm^{-1}-1800 cm^{-1}.

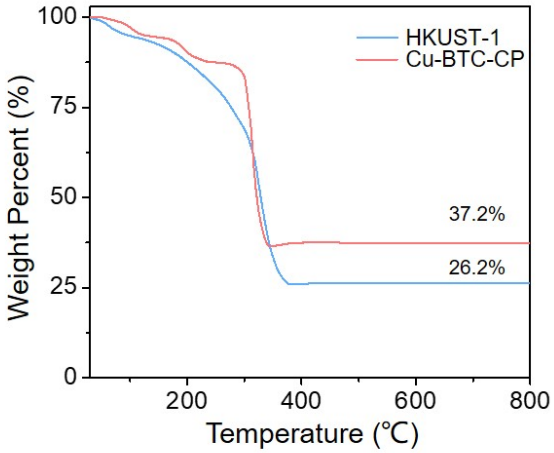

Fig. S6. TG patterns for HKUST-1 and Cu-BTC-CP samples.

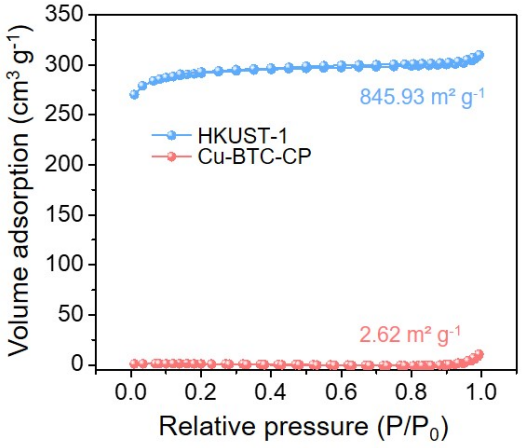

Fig. S7. N_2 adsorption-desorption isotherms of HKUST-1 and Cu-BTC-CP.

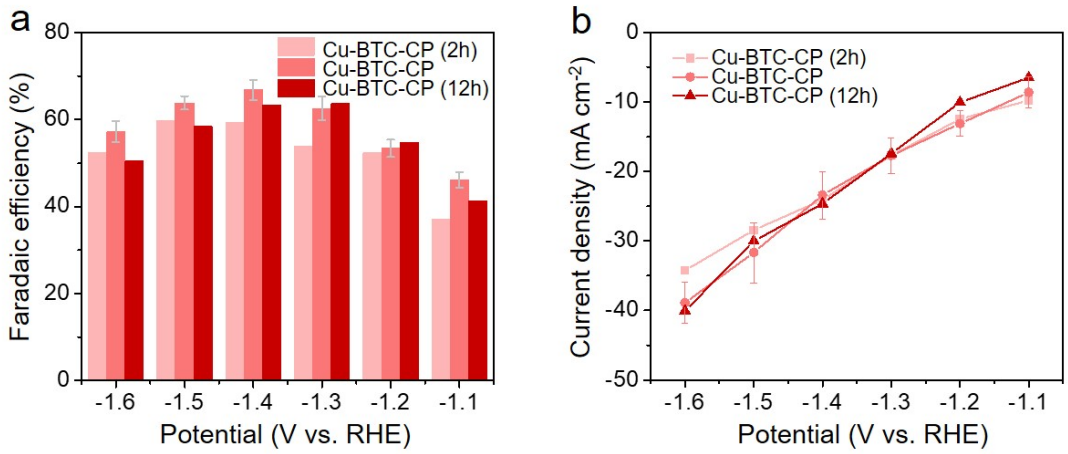

Fig. S8. Potential-dependent (a) FEs of C_2H_4 and (b) total current densities for Cu-BTC-CP (2h), Cu-BTC-CP and Cu-BTC-CP (12h). The potential-dependent gas product distribution indicates the optimized C_2H_4 selectivity and activity for Cu-BTC-CP.

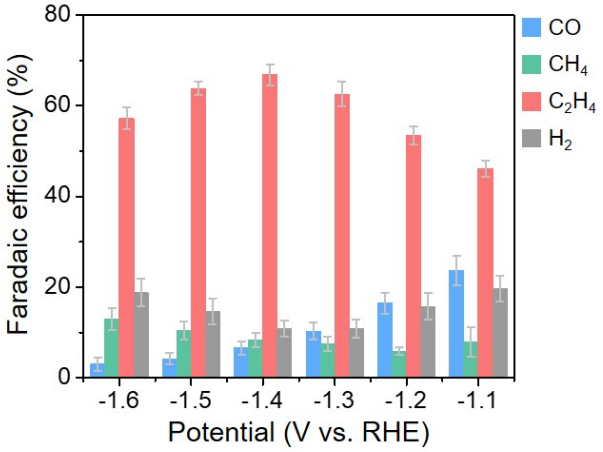

Fig. S9. Potential-dependent FEs of gas products for Cu-BTC-CP in H cell with CO_2-saturated 0.1 M $KHCO_3$, indicating that ethylene is the dominant gas product at the applied potentials.

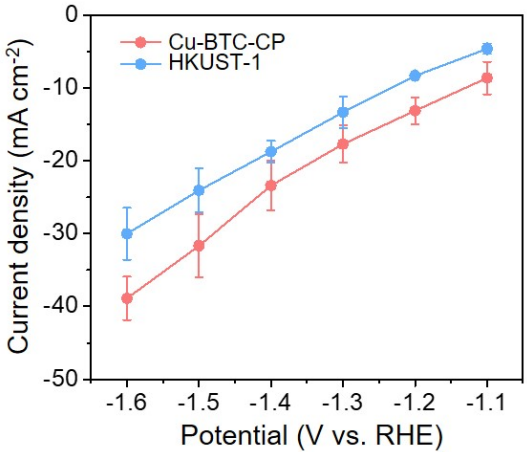

Fig. S10. The potential-dependent total current density for HKUST-1 and Cu-BTC-CP in H cell with CO_2-saturated 0.1 M $KHCO_3$.

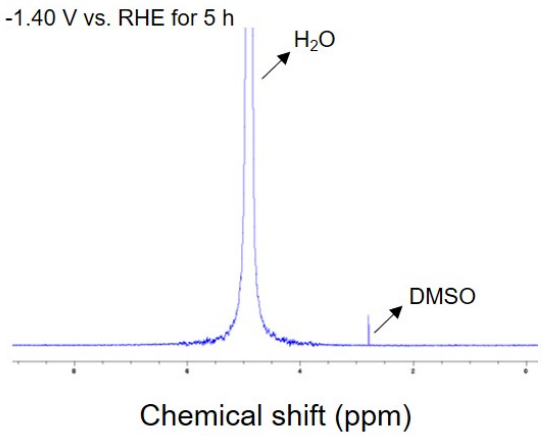

Fig. S11. Representative ^{1}H-NMR spectra of Cu-BTC-CP measured at the potential of –1.40 V vs. RHE in H cell, showing no detectable liquid products. It is mentionable that the liquid products were collected after the reaction runs for 5 h.

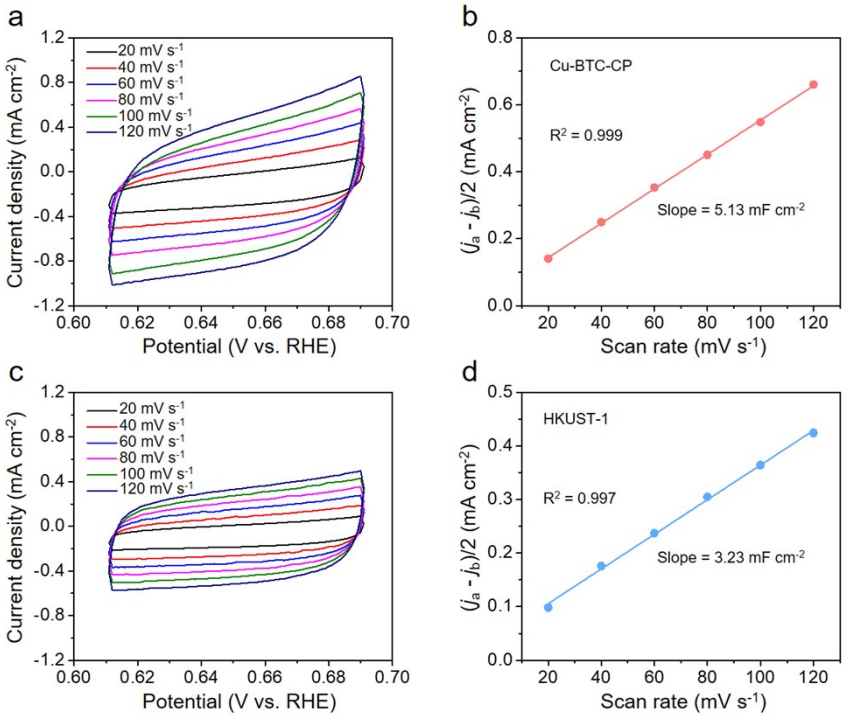

Fig. S12. Cyclic voltammograms measuring in 1 M KOH at scan rates from 20, 40, 60, 80, 100 and 120 mV s^{-1} for (a) Cu-BTC-CP and (c) HKUST-1. The linear slope from CVs for (b) Cu-BTC-CP and (d) HKUST-1, equivalent to twice the double layer capacitance (C_{dl}), was used to represent the ECSA.

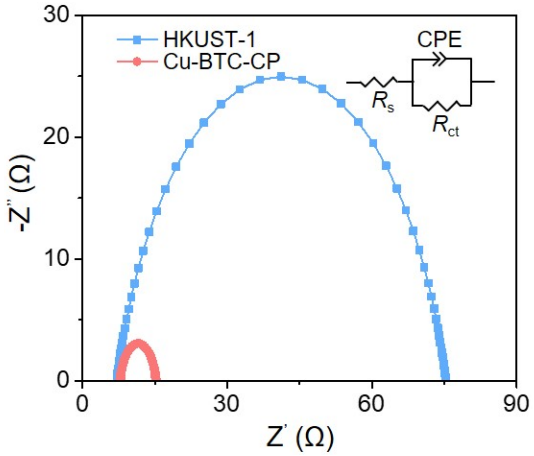

Fig. S13. (a) Nyquist plots of HKUST-1 and Cu-BTC-CP in a flow cell reactor at –0.40 V vs. RHE with 1.0 M KOH, showing the faster electron transfer for the Cu-BTC-CP than that of HKUST-1.

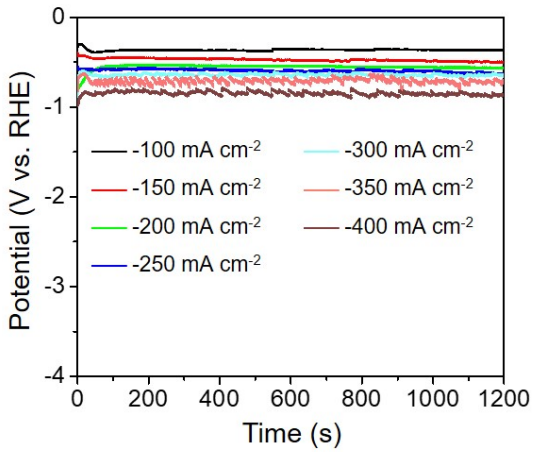

Fig. S14. Chronopotentiometric curves (*iR*-corrected) of Cu-BTC-CP at various applied current densities in a flow cell reactor with 1.0 M KOH.

Note: 90% ohmic resistance correction was applied in all potential. An average resistance of 6.2 Ω was used to calculate the *iR*-corrected.

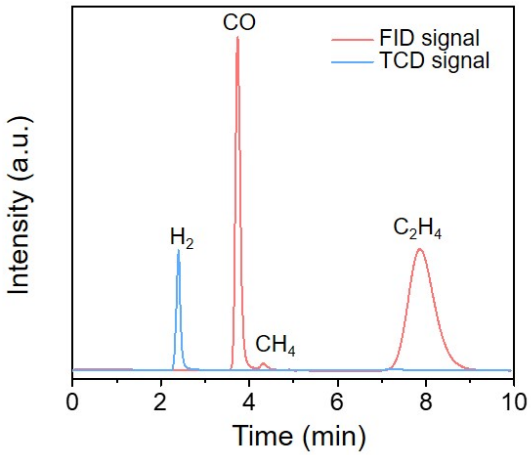

Fig. S15. Typical GC of gas product produced by Cu-BTC-CP at the current density of 350 mA cm^{-2} in a flow cell reactor with 1.0 M KOH.

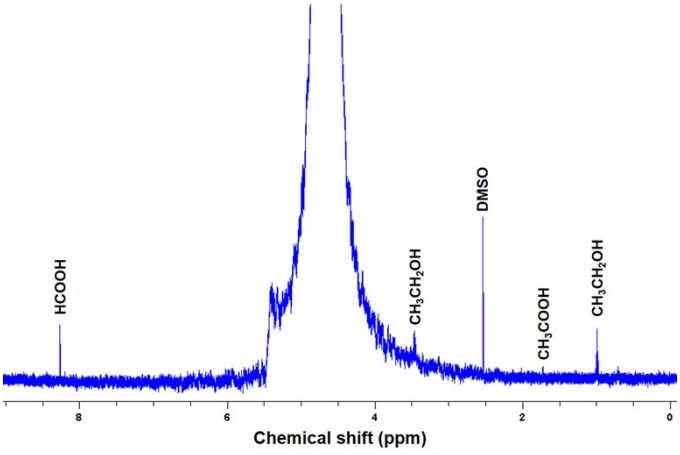

Fig. S16. Representative ^{1}H-NMR spectra of Cu-BTC-CP catalyst measured at 250 mA cm^{-2} in a flow cell reactor with 1.0 M KOH.

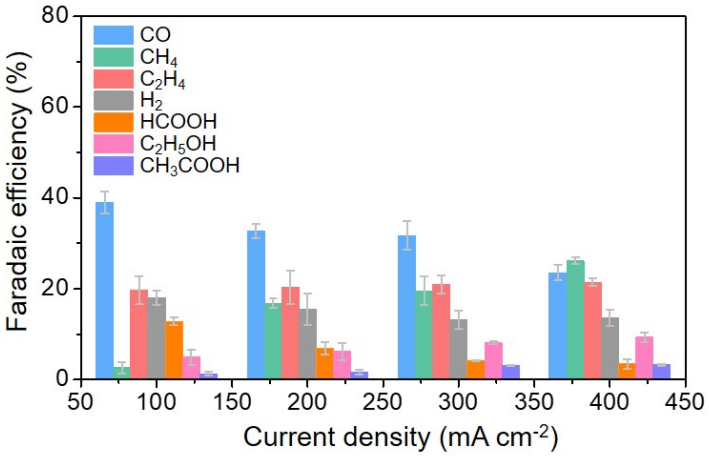

Fig. S17. Current density-dependent FEs for products over HKUST-1 in a flow cell reactor with 1.0 M KOH.

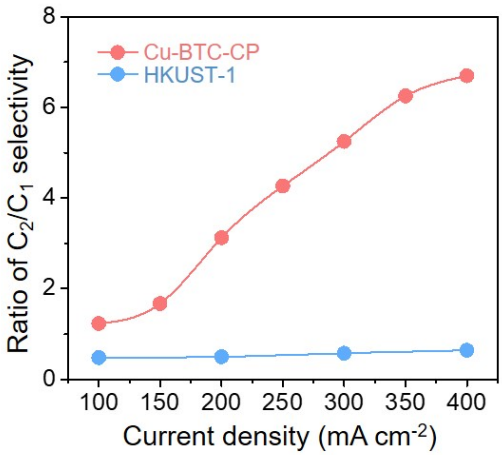

Fig. S18. Plot of C_2/C_1 selectivity ratio versus *j* for HKUST-1 and Cu-BTC-CP.

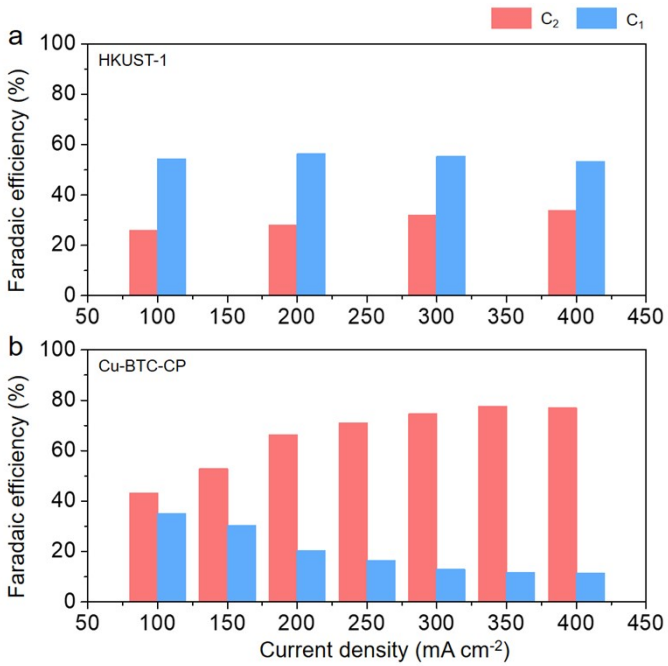

Fig. S19. Current density-dependent FEs of C_1 and C_2 products on (a) HKUST-1 and (b) Cu-BTC-CP in a flow cell reactor with 1.0 M KOH.

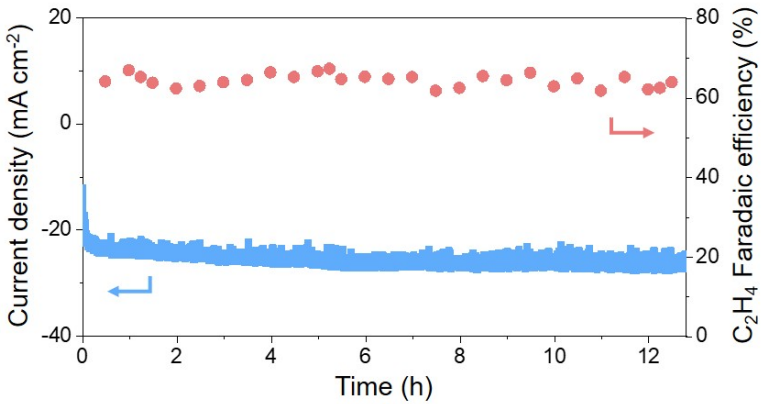

Fig. S20. Stability test of Cu-BTC-CP at a potential of -1.40 V vs. RHE in an H-cell over 12 hours.

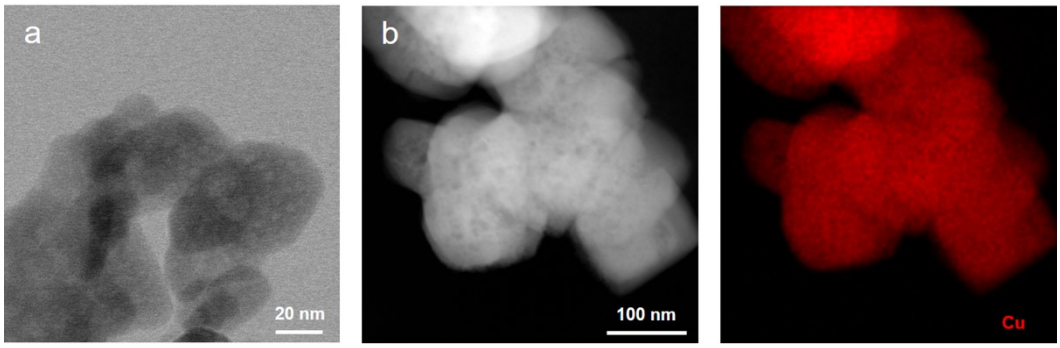

Fig. S21. (a) AC-STEM BF image of Cu-BTC-CP catalyst obtained after CO_2RR electrocatalysis process. (b) HAADF-STEM image of Cu-BTC-CP after CO_2RR and corresponding EDS elemental maps of Cu.

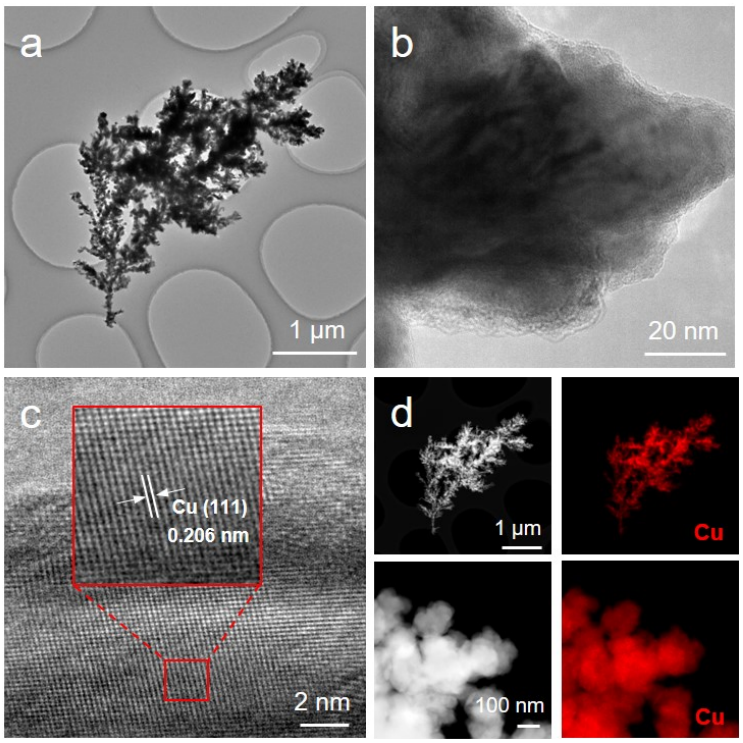

Fig. S22. (a) TEM and (b, c) HRTEM images of HKUST-1 collected after CO_2RR. The insets of (c) are the enlarged HRTEM images, showing the (111) lattice fringe of Cu. (d) HAADF-STEM images of HKUST-1 after CO_2RR in different regions and corresponding EDS elemental maps of Cu.

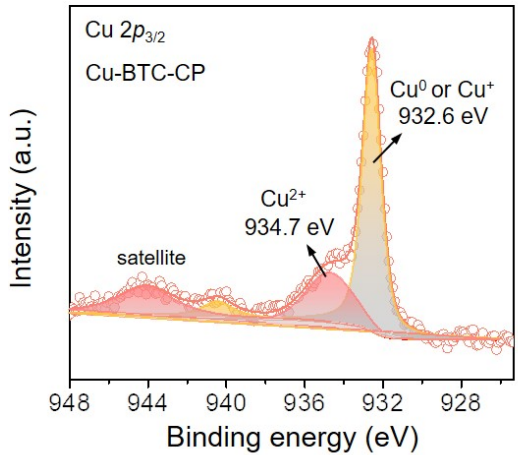

Fig. S23. Cu 2*p* high-resolution XPS spectra of the Cu-BTC-CP catalyst after CO_2RR.

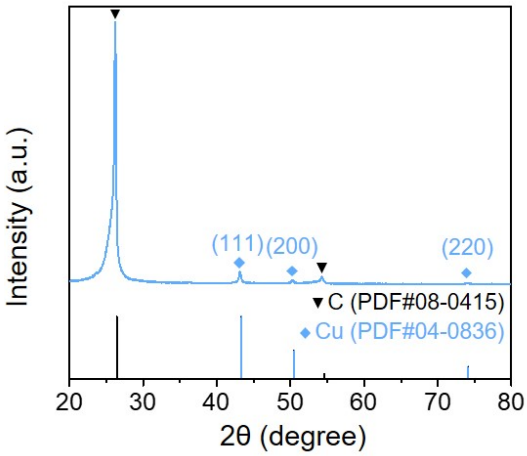

Fig. S24. XRD pattern of HKUST-1 after CO_2RR electrolysis, which proves that the sample has been phase changed into metallic Cu.

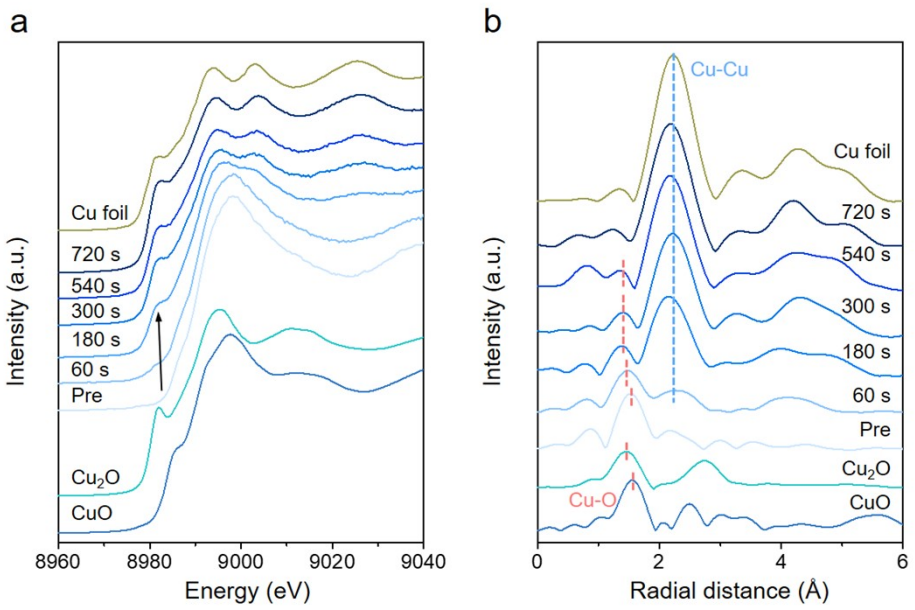

Fig. S25. Reaction time-dependent operando (a) Cu K-edge XANES spectra and (b) Fourier-transformed Cu K-edge EXAFS spectra for HKUST-1 at a potential of –1.30 V vs. RHE. These results indicate that HKUST-1 has been reduced to metallic Cu during the electrolysis.

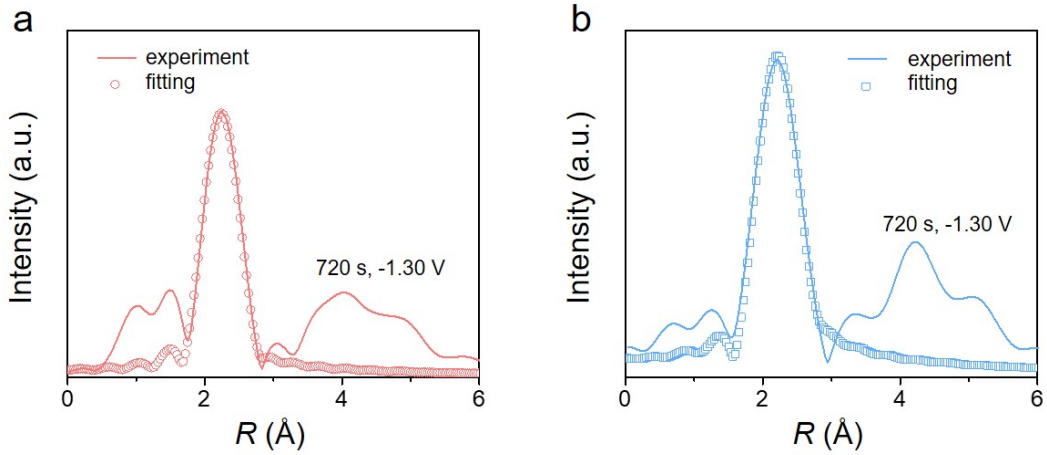

Fig. S26. Fourier-transformed Cu K-edge EXAFS spectra and fitting of the Cu-BTC-CP and HKUST-1 sample at a potential of –1.30 V vs. RHE.

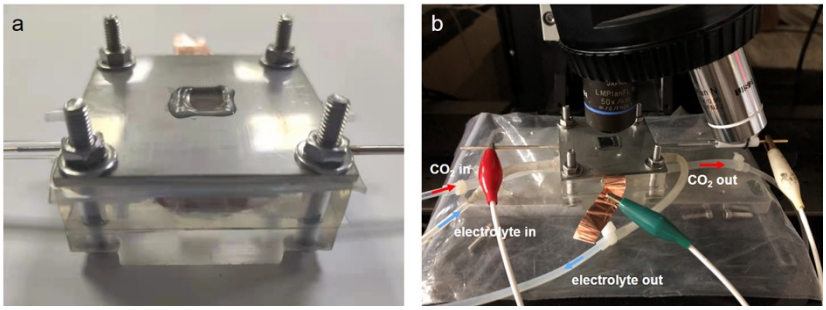

Fig. S27. Digital photograph of the custom-built cell for the *in-situ* Raman characterizations from (a) top-view and (b) in the CO_2RR test state.

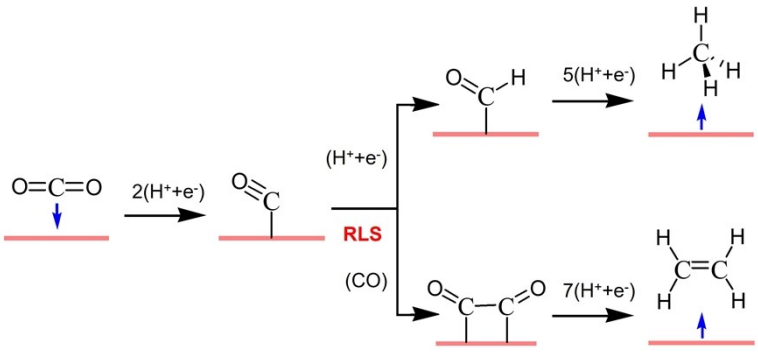

Fig. S28. Schematic for CH_4 and C_2H_4 formation on Cu(111) surface.

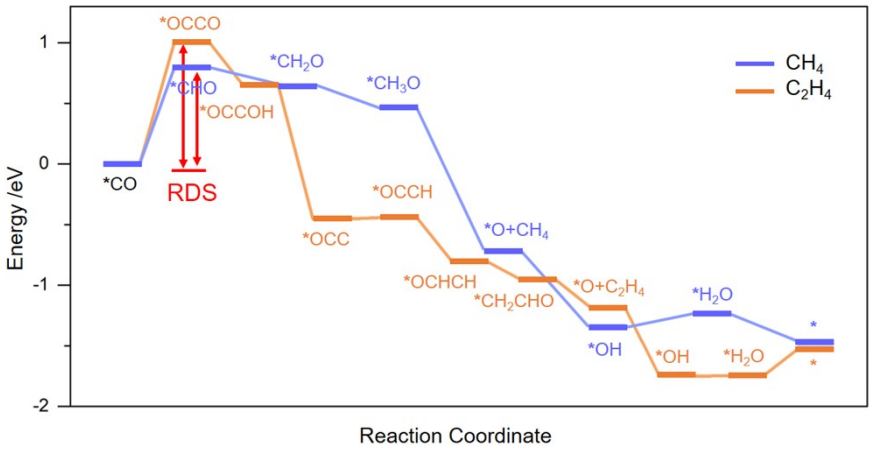

Fig. S29. Free energy of CO_2RR to CH_4 and C_2H_4 at 0 V vs. RHE on Cu(111) surface calculated using the thermochemical model (without solvent water layer).

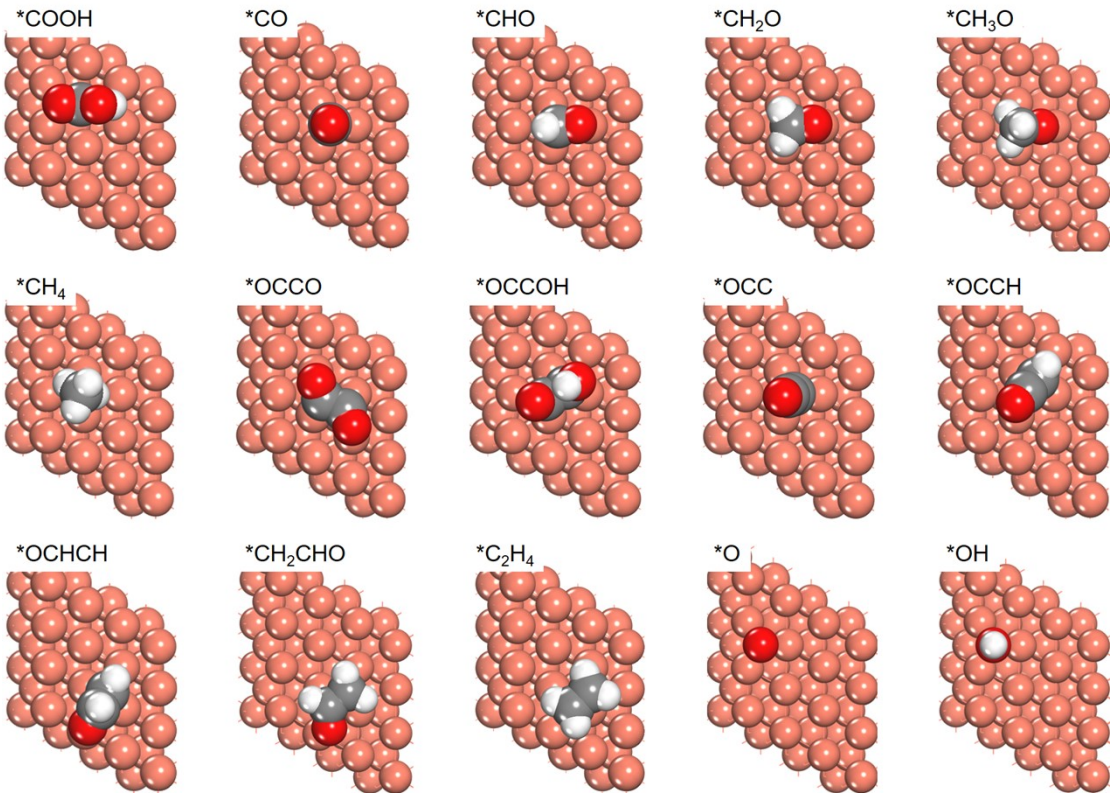

Fig. S30. Optimized geometries of some key intermediates during CH_4 and C_2H_4 formation on Cu(111) surface without considering the solvent effect.

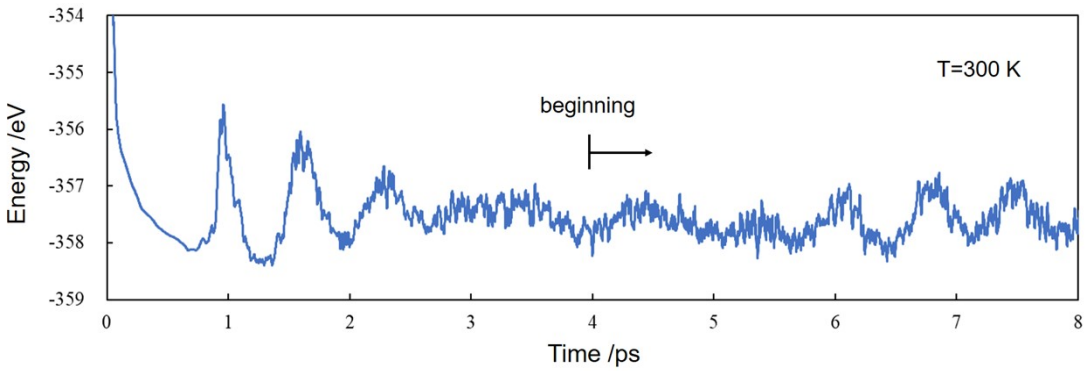

Fig. S31. Energy profile of MD simulation for the Cu system containing solvent water.

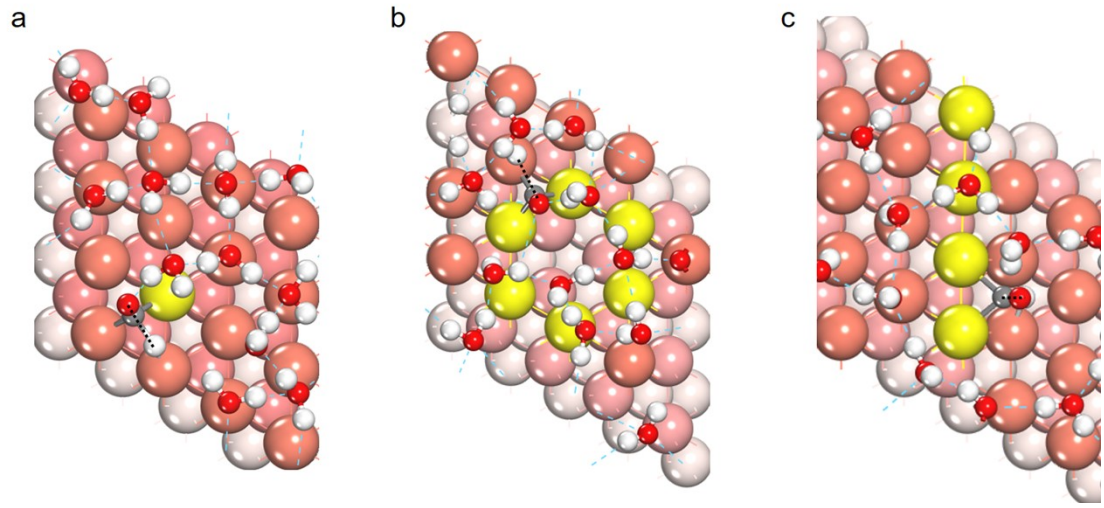

Fig. S32. Transition states of the *CHO intermediate on Cu surface with different CN (CN=9, 8 and 7) considering the solvent effect.

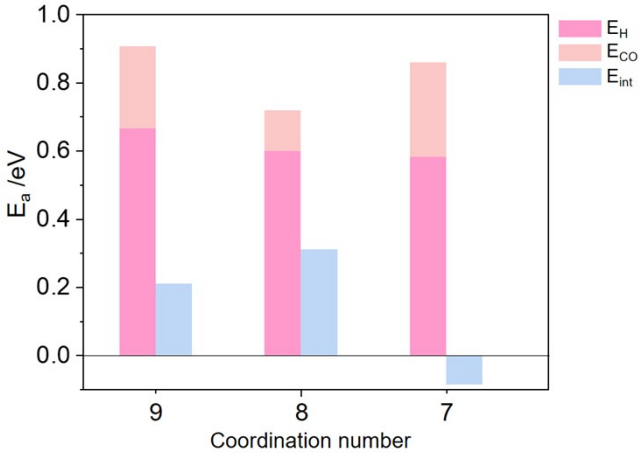

Fig. S33. E_a splitting for CHO formation.

Table S1. Comparison of the performance of recently reported Cu-based metal-organic complex catalysts in electrochemical CO_2 to C_2H_4 conversion.

Catalyst	Potential (V vs. RHE)	η (V)	Partial current density (mA cm^{-2})	FE_{C2H4} (%)	Device	Electrolyte	References
Cu-BTC-CP	–0.73*	–0.81	228.20	65.2 ± 3	Flow cell	1 M KOH	This work
	–1.40	–1.48	15.63	66.8 ± 2	H cell	0.1 M $KHCO_3$	
Cu-PzH	–1.00*	–1.08	346.46	56.0 ± 4.97	Flow cell	1 M KOH	11
Cu_3-Br	–0.70*	–0.78	73.24	55.0	Flow cell	0.5 M KOH	12
Cu dimer distorted HKUST-1	–1.07*	–1.15	117.90	45.0	Flow cell	1 M KOH	13
PcCu-Cu-O	–1.20	–1.28	3.70	50.0	H cell	0.1 M $KHCO_3$	14
Cu_2BDC	–1.30	–1.38	/	< 35.0	H cell	0.1 M KCl	15
KB@Cu_3(HITP)$_2$	–1.37*	–1.45	26.50	~70.0	H cell	0.1 M $KHCO_3$	16
	–0.93*	–1.01	305.00	51.0	Flow cell	1 M KOH	
BIF-102NSs	–1.00	–1.08	/	11.3	H cell	0.5 M $KHCO_3$	17
CuBtz	–1.30	–1.38	5.80	44.0	H cell	0.1 M $KHCO_3$	18
	–1.60	–1.68	582.00	~20.0	Flow cell	1 M KOH	
Cu-ade	–1.40	–1.48	8.50	45.0	H cell	0.1 M $KHCO_3$	19

Cu(111)@Cu THQ	–1.40	–1.48	6.00	42.0	H cell	0.1 M $KHCO_3$	20
PorCu	–0.97*	–1.05	8.33	17.0	H cell	0.5 M $KHCO_3$	21
Cu phthalocyanine	–1.60	–1.68	2.80	25.0	H cell	0.5 M KCl	22
Cu(OH)BTA	–0.87*	–0.95	285	57.0	Flow cell	1 M KOH	23

Notes: * means the potentials were *iR*-corrected. $\eta = E_{appl} - E^0$, where η is overpotential, E_{appl} is applied potential and E^0 is equilibrium potential ($E(_{C2H4})^0 = 0.08$ V vs. RHE).[24, 25]

Table S2. Fitting parameters of Cu K-edge EXAFS spectra of the Cu-BTC-CP and HKUST-1 at –1.30 V vs. RHE.

Sample	Reaction time	Cu-Cu		$\sigma^2(10^{-3}$ Å$^2)$	ΔE_0(eV)	*R*-factor
		CN	*R*(Å)			
Cu-BTC-CP	720s	8.0	2.55	8.8	4.2	0.011
HKUST-1	720s	9.0	2.54	7.2	2.6	0.016

Notes: *CN*, coordination number; *R*, distance; ΔE_0, energy shift; σ^2, Debye-Waller factor.

Table S3. Free energies (ΔG in eV) of the CO_2RR to CH_4 and C_2H_4 for the elementary steps involved over Cu(111) surface without considering solvent effect.

	Reaction process	Cu(111)
Form-CH_4	$^*CO + (H^+ + e^-) \rightarrow {}^*CHO$	0.80
	$^*CHO + (H^+ + e^-) \rightarrow {}^*CH_2O$	-0.16
	$^*CH_2O + (H^+ + e^-) \rightarrow {}^*CH_3O$	-0.18
	$^*CH_3O + (H^+ + e^-) \rightarrow {}^*O + CH_4$	-0.18
Form-C_2H_4	$2^*CO \rightarrow {}^*OCCO + *$	1.01
	$^*OCCO + (H^+ + e^-) \rightarrow {}^*OCCOH$	-0.37
	$^*OCCOH + * \rightarrow {}^*OCC + {}^*OH$	-1.10
	$^*OCC + (H^+ + e^-) \rightarrow {}^*OCCH$	0.01
	$^*OCCH + (H^+ + e^-) \rightarrow {}^*OCHCH$	-0.36
	$^*OCHCH + (H^+ + e^-) \rightarrow {}^*CH_2CHO$	-0.16
	$^*CH_2CHO + (H^+ + e^-) \rightarrow {}^*O + C_2H_4$	-0.23
Form-H_2O	$^*O + (H^+ + e^-) \rightarrow {}^*OH$	-0.57
	$^*OH + (H^+ + e^-) \rightarrow {}^*H_2O$	0.10
	$^*H_2O \rightarrow H_2O + *$	0.15

Table S4. Activation energy barrier (E_a) of *CO hydrogenation (i.e., $^*CO + (H^+ + e^-) \rightarrow {}^*CHO$) and dimerization (i.e., $2^*CO \rightarrow {}^*OCCO + *$) in different CN (CN=9, 8 and 7).

CN	$^*CO + (H^+ + e^-) \rightarrow {}^*CHO$	$2^*CO \rightarrow {}^*OCCO + *$
9	1.12	0.88
8	1.03	0.59
7	0.77	0.69

Table S5. Decomposition of activation energies for *CO hydrogenation and dimerization on Cu(111) surface with different CN.

CN	OCCO			CHO		
	E_{A1}	E_{A2}	E_{int}	E_H	E_{CO}	E_{int}
9	0.32	0.38	0.18	0.67	0.24	0.21
8	0.49	0.46	-0.36	0.60	0.12	0.31
7	0.19	0.70	-0.21	0.58	0.28	-0.08

References

1. G. Kresse and J. Furthmüller, *Phys. Rev. B*, 1996, **54**, 11169-11186.

2. G. Kresse and J. Furthmüller, *Comp. Mater. Sci.*, 1996, **6**, 15-50.

3. J. P. Perdew, A. Ruzsinszky, G. I. Csonka, O. A. Vydrov, G. E. Scuseria, L. A. Constantin, X. Zhou and K. Burke, *Phys. Rev. Lett.*, 2008, **100**, 136406.

4. J. P. Perdew, K. Burke and M. Ernzerhof, *Phys. Rev. Lett.*, 1996, **77**, 3865-3868.

5. G. Kresse and D. Joubert, *Phys. Rev. B*, 1999, **59**, 1758-1775.

6. S. Grimme, J. Antony, S. Ehrlich and H. Krieg, *J. Chem. Phys.*, 2010, **132**, 154104.

7. H. Yuan, N. Sun, J. Chen, J. Jin, H. Wang and P. Hu, *ACS Catal.*, 2018, **8**, 9269-9279.

8. M. Zhou and H.-F. Wang, *Chin. Chem. Lett.*, 2022, **33**, 4705-4709.

9. J. Xing, H. B. Jiang, J. F. Chen, Y. H. Li, L. Wu, S. Yang, L. R. Zheng, H. F. Wang, P. Hu, H. J. Zhao and H. G. Yang, *J. Mater. Chem. A*, 2013, **1**, 15258-15264.

10. W. Zhang, C. Huang, J. Zhu, Q. Zhou, R. Yu, Y. Wang, P. An, J. zhang, M. Qiu, l. Zhou, L. Mai, Z. Yi and Y. Yu, *Angew. Chem. Int. Ed.*, 2022, **61**, e202112116.

11. R. Wang, J. Liu, Q. Huang, L. Z. Dong, S. L. Li and Y. Q. Lan, *Angew. Chem. Int. Ed.*, 2021, **60**, 19829-19835.

12. Y. Q. Lan, Y. F. Lu, L. Z. Dong, J. Liu, R. X. Yang, J. J. Liu, Y. Zhang, L. Zhang, Y. R. Wang and S. L. Li, *Angew. Chem. Int. Ed.*, 2021, **133**, 26414-26421.

13. D.-H. Nam, O. S. Bushuyev, J. Li, P. De Luna, A. Seifitokaldani, C.-T. Dinh, F. P. Garcia de Arquer, Y. Wang, Z. Liang, A. H. Proppe, C. S. Tan, P. Todorovic, O. Shekhah, C. M. Gabardo, J. W. Jo, J. Choi, M. J. Choi, S.-W. Baek, J. Kim, D. Sinton,

S. O. Kelley, M. Eddaoudi and E. H. Sargent, *J. Am. Chem. Soc.*, 2018, **140**, 11378-11386.

14. X.-F. Qiu, H.-L. Zhu, J.-R. Huang, P.-Q. Liao and X.-M. Chen, *J. Am. Chem. Soc.*, 2021, **143**, 7242-7246.

15. X. Zhou, J. Dong, Y. Zhu, L. Liu, Y. Jiao, H. Li, Y. Han, K. Davey, Q. Xu, Y. Zheng and S. Z. Qiao, *J. Am. Chem. Soc.*, 2021, **143**, 6681-6690.

16. H. Sun, L. Chen, L. Xiong, K. Feng, Y. Chen, X. Zhang, X. Yuan, B. Yang, Z. Deng, Y. Liu, M. H. Rummeli, J. Zhong, Y. Jiao and Y. Peng, *Nat. Commun.*, 2021, **12**, 6823.

17. P. Shao, W. Zhou, Q. L. Hong, L. Yi, L. Zheng, W. Wang, H. X. Zhang, H. Zhang and J. Zhang, *Angew. Chem. Int. Ed.*, 2021, **60**, 16687-16692.

18. H. L. Zhu, H. Y. Chen, Y. X. Han, Z. H. Zhao, P. Q. Liao and X. M. Chen, *J. Am. Chem. Soc.*, 2022, **144**, 13319-13326.

19. F. Yang, A. Chen, P. L. Deng, Y. Zhou, Z. Shahid, H. Liu and B. Y. Xia, *Chem. Sci.*, 2019, **10**, 7975-7981.

20. Z. H. Zhao, K. Zheng, N. Y. Huang, H. L. Zhu, J. R. Huang, P. Q. Liao and X. M. Chen, *Chem. Commun.*, 2021, **57**, 12764-12767.

21. Z. Weng, J. Jiang, Y. Wu, Z. Wu, X. Guo, K. L. Materna, W. Liu, V. S. Batista, G. W. Brudvig and H. Wang, *J. Am. Chem. Soc.*, 2016, **138**, 8076-8079.

22. S. Kusama, T. Saito, H. Hashiba, A. Sakai and S. Yotsuhashi, *ACS Catal.*, 2017, **7**, 8382-8385.

23. Y. Liang, J. Zhao, Y. Yang, S. F. Hung, J. Li, S. Zhang, Y. Zhao, A. Zhang, C.

Wang, D. Appadoo, L. Zhang, Z. Geng, F. Li and J. Zeng, *Nat. Commun.*, 2023, **14**, 474.

24. Y. Y. Birdja, E. Pérez-Gallent, M. C. Figueiredo, A. J. Göttle, F. Calle-Vallejo and M. T. M. Koper, *Nat. Energy*, 2019, **4**, 732-745.

25. S. Nitopi, E. Bertheussen, S. B. Scott, X. Liu, A. K. Engstfeld, S. Horch, B. Seger, I. E. L. Stephens, K. Chan, C. Hahn, J. K. Norskov, T. F. Jaramillo and I. Chorkendorff, *Chem. Rev.*, 2019, **119**, 7610-7672.